PROCEEDINGS, 50th Workshop on Geothermal Reservoir Engineering
Stanford University, Stanford, California, February 10-12, 2025
SGP-TR-229

Petrologic Validation of Exploration Geophysical Anomalies Utilizing Drill Core and Cuttings from the Don A. Campbell Geothermal System, Nevada, USA

Kurt O. Kraal[1], Mathew Folsom[2], Carmen Winn[2], Daniel Feucht[3], Ben Delwiche[3], Nicholas Hinz[2], William Cumming[5] Steve Sewell[4], & Christine Downs[1]

[1]Sandia National Laboratories, 1515 Eubank Blvd SE, Albuquerque, NM, 87123

[2] Geologica Geothermal Group Inc.

[3]Ormat Technologies Inc.

[4]Australis Geoscience Ltd.

[5]Cumming Geoscience.

E-mail: kokraal@sandia.gov

Keywords: Clay Cap, Smectite, BRIDGE, Silicification, Resistivity, HTEM, SWIR, Infrared Spectroscopy

ABSTRACT

Blind or hidden geothermal systems have been identified as a potentially underutilized source of renewable energy in the Great Basin region of the western USA. Because discovery of these resources is difficult, methodologies and techniques to detect hidden geothermal resources are an active research area. Several geophysical anomalies have been found to be associated with resource-capable geothermal systems in the Great Basin region, including shallow low resistivity, near surface densification (as observed with gravity data), and a magnetic low. These features are inferred to be products of hydrothermal alteration, however, validation of this interpretation through analysis of subsurface samples is lacking in the geothermal exploration literature for moderate temperature (~120-180 °C) deep circulation-type systems commonly found in the Great Basin (as opposed to relatively high-temperature (>200 °C) magmatically heated geothermal systems hosted in volcanic environments). Here we present results of petrologic analysis of core and cuttings from the Don A. Campbell geothermal system (resource temperature ~130 °C hosted in basin-fill sediments) to validate our interpretation of Helicopter Transient Electromagnetic Data (HTEM) collected over the site. Methods utilized are sample inspection, infrared reflectance spectroscopy in the Short-Wave InfraRed range (SWIR), and Methylene-Blue (MeB) analysis to estimate smectite abundance. These new data are also compared to existing geologic, geophysical, and temperature data, as well as the natural state resource conceptual model for the site. We found the presence of several hydrothermal alteration minerals, including smectite, interlayered illite-smectite, kaolinite, silica, carbonate, hematite, and pyrite. These minerals are found with a distinct zonation, including a shallow argillic zone, a shallow silica-carbonate-pyrite-illite-smectite zone embedded within the argillic zone, a deeper silica-carbonate-pyrite-illite-smectite with minor chlorite zone, and a shallow kaolinite-smectite-hematite zone near the water table. The relative smectite content of each of these zones appear to be captured by the HTEM, with low-resistivity (~3-5 ohm.m) zones collocated with the argillic zone containing 5-13 % smectite, and relatively high-resistivity values (~5-7.5 ohm.m) colocated with the silica-carbonate-pyrite-illite-smectite zones with smectite contents of less than 3%. In addition, the highest values in the first vertical derivative of the gravity data, inferred to be due to near-surface densification, correspond to the shallow silicified zone identified in the core. Finally, we discuss the implications of this study for exploration for hidden geothermal systems in the Great Basin and analogous regions.

1. INTRODUCTION

Several geophysical methods (e.g. resistivity, gravity, magnetics) are commonly utilized for site characterization during geothermal exploration, typically where a temperature anomaly is known. Recently, resistivity methods have begun to be utilized for green-field exploration in the Great Basin region, with the acquisition of regional Helicopter Transient ElectroMagnetic (HTEM) data by the BRIDGE project (Figure 1), and current acquisition by the U.S. Geological Survey as part of the Earth-MRI program. These large publicly funded data acquisitions have the potential to lead to new green-field geothermal discoveries. The use of resistivity for green-field exploration is informed by a conceptual model in which shallow (0-500 m) low-resistivity zones in unconsolidated alluvial sediments with characteristic geometries are consistent with smectite-clay formed through hydrothermal alteration processes overlying and adjacent to known geothermal systems (Sewell et al., 2023; Downs et al., 2025). Low-resistivity zones due to smectite alteration are found "capping" many high-temperature (>200 °C) geothermal resources hosted in volcanic environments (e.g. Ussher et al., 2000). Despite similar low-resistivity zones observed above or adjacent to moderate temperature (130-200 °C) deep-circulation type systems in the Great Basin region (e.g. at Desert Peak, San Emidio, Brady's, Dixie Meadows, Tungsten Mountain, Steamboat; Benoit et al., 1982; Folsom et al., 2018; 2020; Delwiche et al., 2023; Feucht et al., 2023), the nature and cause of the zone remains underexplored in deep circulation type resources. In addition, the application of HTEM has found additional complexity in shallow resistivity geometries, often missed in coarser MT data (e.g. Folsom et al., 2024) that could be investigated further. Gravity methods are utilized both for understanding geologic structure in basins, and identifying near-surface densification, inferred to be caused by silicification by

hydrothermal fluids (e.g. San Emidio; Folsom et al., 2020). Lastly, magnetics can be used to infer geologic structure, as well as identifying areas of possible hydrothermal alteration leading to the destruction of magnetic minerals, producing magnetic lows (Allis, 1990).

In order to better understand these geophysical tools, we conducted a petrologic investigation of drill core and cuttings that intersect these geophysical features. One location with an abundance of available geologic, geophysical, and well data is the Don A. Campbell (DAC) geothermal system in western Nevada, operated by Ormat Technologies, Inc. (Figure 1). The goal of this paper is to validate the interpretation of the HTEM data acquired over the site by the BRIDGE project by petrologic investigations of several geothermal wells and boreholes from the site. In this pilot project, we performed sample inspection, infrared reflectance spectroscopy analysis, and Metheleyne-blue analysis of drill core or cuttings from four wells. Follow up work could include petrographic microscopy, XRD analysis, and measurement of petrophysical properties (such as resistivity, density, magnetic susceptibility) for further validation.

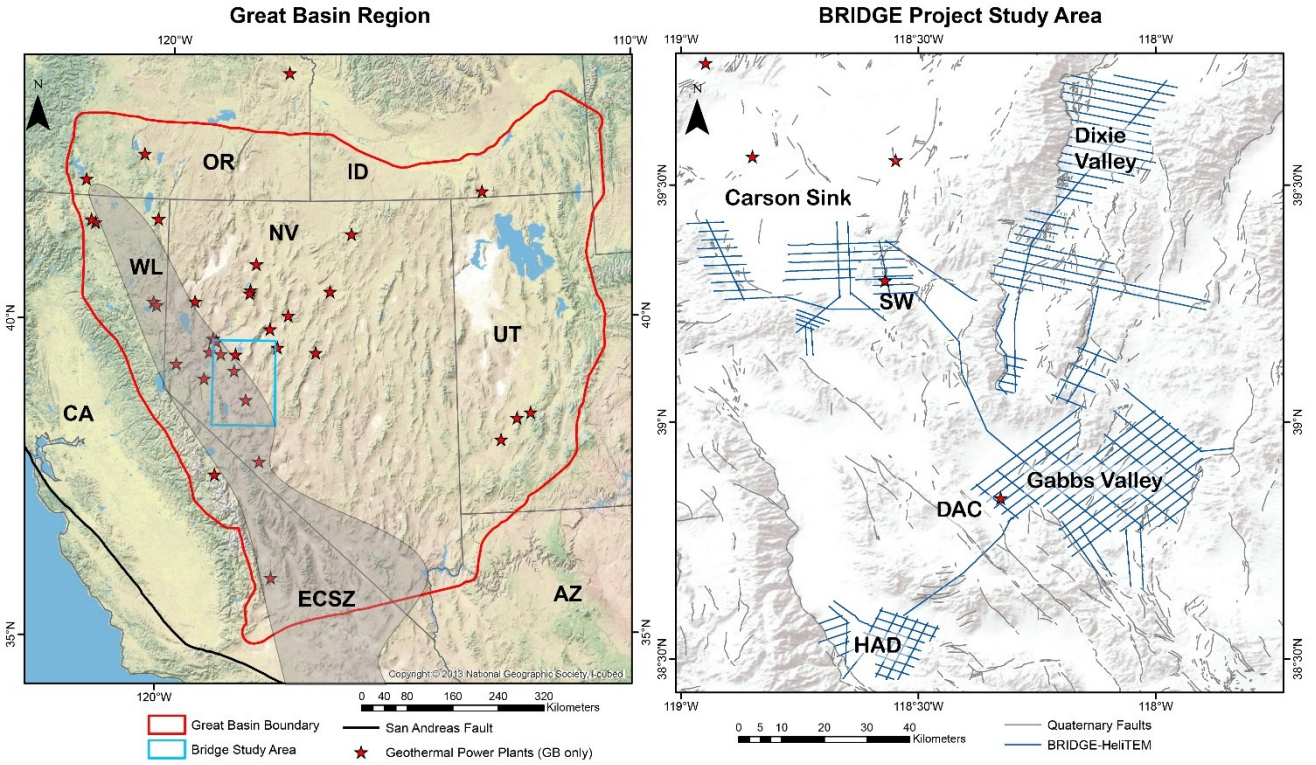

Figure 1: Left: Regional location of Great Basin (GB) region of the western USA, including the Walker Lane (WL) and Eastern California Share Zone (ECSZ), and the BRIDGE project study area. Right: Bridge project study area with locations of BRIDGE HeliTEM (HTEM) data acquisition, major basins investigated, and the location of the Don A. Campbell (D.A.C.) geothermal system. Also shown is the Salt Wells (SW) geothermal system location, and the Hawthorne Army Depot (HAD).

2. BACKGROUND

The Don A. Campbell (DAC) geothermal resource is located in Gabbs Valley of western Nevada. Gabbs Valley is within a transition between the Walker Lane, characterized by NW-striking dextral transtension that accommodates ~20% of the relative plate motion between the North American and Pacific Plates, and the Basin and Range province, characterized by northwest-southeast extension accommodated by northeast-striking normal faults (Figure 1). In addition to DAC, several other temperature anomalies have been identified in the basin, including the Petrified Springs geothermal system in southeast Gabbs Valley (Craig et al., 2021), Cobble Cuesta (Payne, 2013), North Gabbs (Kratt et al., 2008), and several additional hot wells near the town of Gabbs (Downs et al., 2023).

The discovery of the DAC geothermal resource was through mining of mineral exploration data from the early 1990s that identified a magnetic-low anomaly, hydrothermal alteration minerals such as clay, pyrite, chalcedony, and chlorite, and 88 °C (190 °F) fluids at depths between 50-500 ft (Orenstein & Delwiche, 2014). Based on these, Ormat nominated this property to the BLM's competitive geothermal lease auction in 2001, and secured site control in 2007 (Orenstein & Delwiche, 2014). Ormat then commenced an exploration campaign, which included collection and interpretation of geoscientific data, drilling, and well production-injection testing. Following exploration, Ormat designed and installed a >16 MW (net) binary geothermal power plant that began production in 2013 (Orenstein & Delwiche, 2014). As of February 2024, DAC has a generating capacity of 30 MW.

The DAC geothermal resource is located within a displacement transfer zone consisting of a series of northwest-striking oblique slip faults separated by northwest striking normal faults, some dipping to the northwest and others to the southeast (Delwiche, 2013; Figure

2A). A shallow (2-m) temperature survey conducted by Kratt et al. (2010) outlined a 6 km^2 zone of elevated temperatures with maximum measured temperatures of 37 °C (19.3 °C relative to local background conditions; Figure 2A) consistent with and expanding the shallow temperature anomaly defined by the early exploration wells. A gravity survey contracted by Ormat identified shallow densification, as visible in the first vertical derivative (1VD) of the gravity data that is co-located with the shallow thermal anomaly (Feucht et al., 2024); Figure 2C). Earlier magnetic data, as well as recent regional aeromagnetic data acquired as part of the GeoDAWN survey (Glen & Earney, 2024) reveal a magnetic low that is also co-located with the shallow temperature anomaly, and the shallow densification as observed in the gravity data (Figure 2D). Finally, the shallow resistivity data collected using HTEM by the BRIDGE project indicates a shallow (<100 m) conductor that is also co-located with the field as outlined by the shallow temperature data, exploration data, and the existing geophysical surveys (Sewell et al., 2023; Figure 2B).

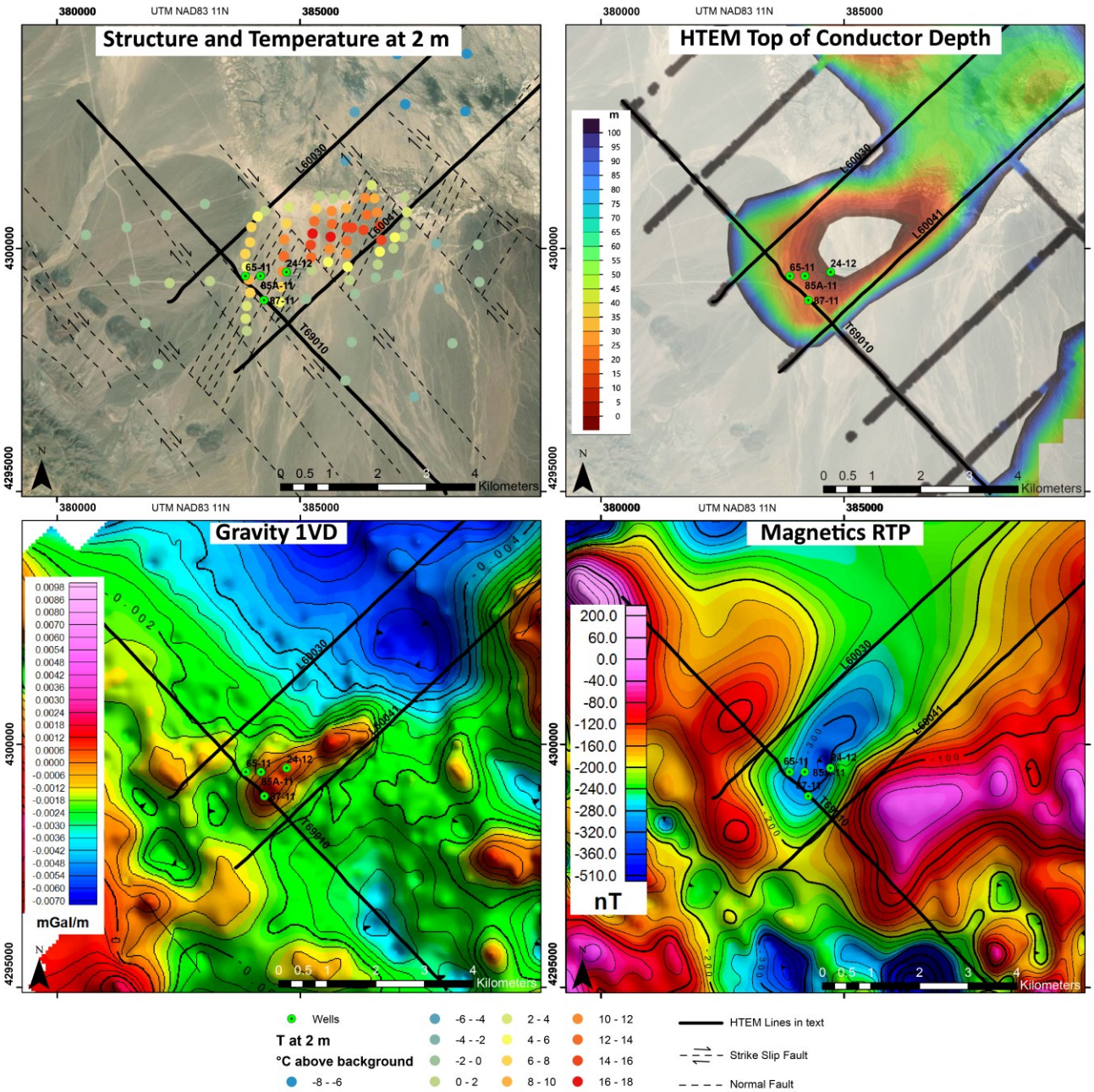

Figure 2: Maps of Don Campbell showing geophysics, cross section line, and well locations (for wells referenced in the text). Faults adapted from Delwiche (2013), 2-m temperature survey from Kratt et al., (2010), HTEM from Sewell et al., (2023), gravity 1VD from Feucht et al. (2024), and magnetics from GeoDAWN (Glen and Earney, 2024).

Three of the BRIDGE HTEM lines (L69010E, L60041N, L60030N) cross over the DAC geothermal resource (Figure 2, Figure 3). L69010E runs roughly parallel to the northwest-striking oblique slip faults and crosses closest to the production wells currently in use at DAC (Figure 2). This line features a low resistivity zone (<3 ohm.m) at shallow depths (30 – 250 m) that is collocated with the magnetic low from GeoDAWN and the high in the Gravity 1VD (Figure 4). A portion of the shallow low resistivity zone in L69010E contains an

embedded resistive zone (Figure 3). A portion of the HTEM data from this line was unusable where the instrument crossed power plant infrastructure at DAC (shown as a vertical white area). L60041N is perpendicular to L69010E and runs roughly parallel to the northwest striking normal faults just to the southeast of the wellfield (Figure 2). The HTEM section shows two domal-shaped shallow low resistivity zones that are divided by a northeast-striking oblique slip fault (Figure 2; Figure 3). L60030N is parallel to L60041N, and passes just to the northwest of the DAC wellfield (Figure 2). This line also has a shallow low resistivity zone, including a double conductive body with an embedded resistive body (Figure 3). Because L69010E most directly crosses the resource, existing geothermal wells, and the geophysical anomalies of interest, we will restrict our discussion to this line primarily for the purposes of this study.

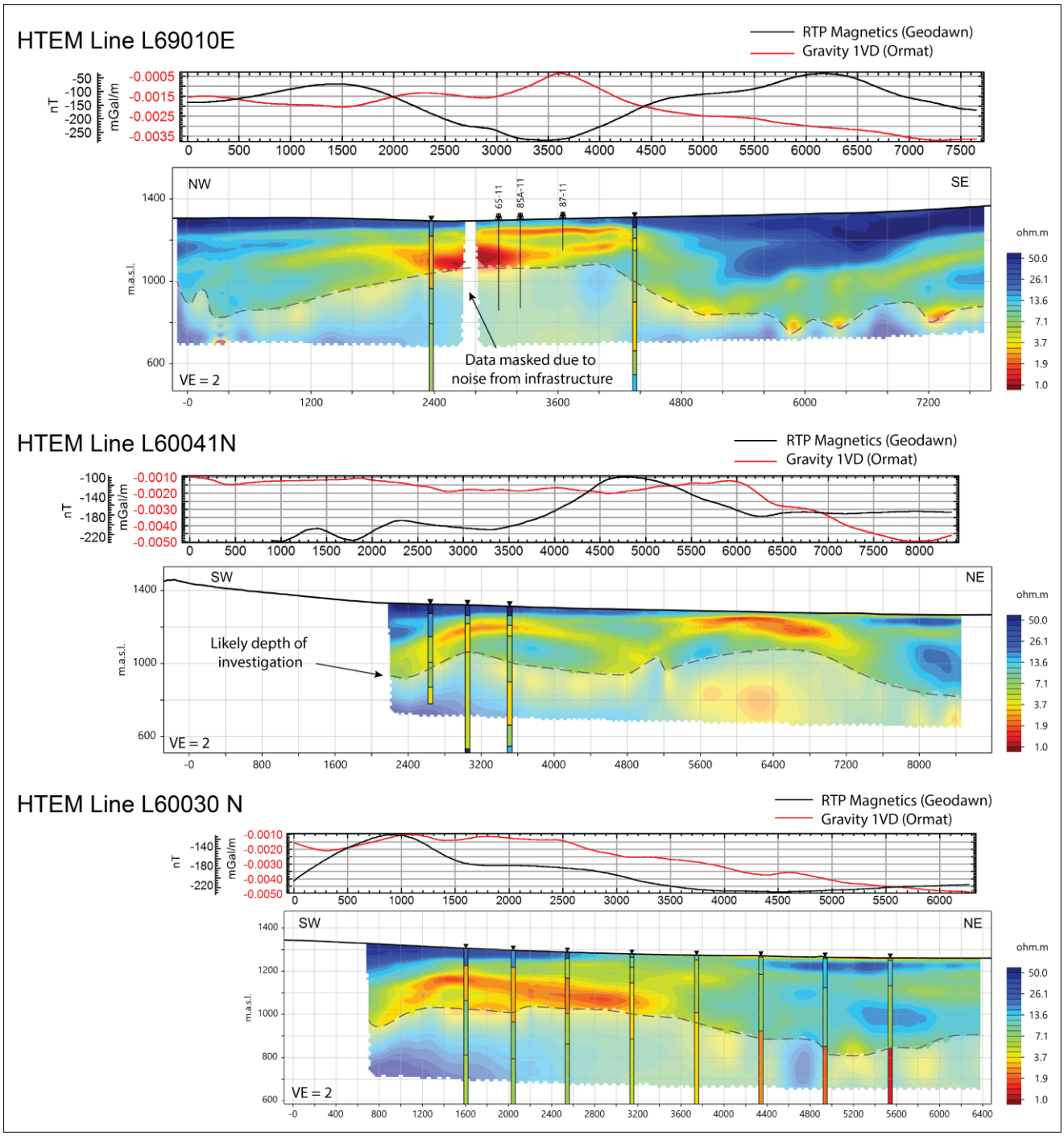

Figure 3: HTEM cross sections discussed in the paper overlain by 1D stick models of the TE model of Ormat's MT data, as well as geophysical profiles: gravity 1VD (Ormat) and Magnetics RTP residual (Geodawn) along the HTEM lines. The HTEM likely depth of investigation is shown by a dashed line following the methods of Vest Christiansen & Auken (2012). See Figure 2 for section line locations.

The general conceptual model is based on Ormat proprietary data, and presented previously in Delwiche (2013), Orenstein & Delwiche (2014; 2015), and discussed in Winn et al. (2021; 2023) and Feucht et al. (2024) is presented in Figure 4 along the BRIDGE HTEM line 69010 E, with inferred natural state isotherms from downhole temperature logs of several wells, and geology from Delwiche (2013). The currently exploited resource at DAC is hosted in Quaternary basin fill sediments (poorly sorted sands, gravel, silt and clay) that are hydrothermally altered (Delwiche, 2013; Orenstein & Delwiche 2014). Upflow to the Quaternary basin fill sediments from deeper Tertiary volcanics and inferred Mesozoic basement rocks is inferred to occur along fractures zones created by the southwest-striking northwest-dipping normal faults. Deep exploration drilling indicates that the basement is relatively low permeability compared to the basin fill sediments, as evident from higher (conductive) temperature gradients. The shallow reservoir consists of fluids at temperatures between ~120-130 °C (Figure 4). Our interpretation of fluid flow pathways presented in Figure 4 differs from previous models in that we posit an additional shallow outflow near well 87-11 that may or may not be separate from the deeper reservoir hosted in basin fill sediments, and this will be discussed further in the text. The low-resistivity zones observed in the HTEM correspond to relatively closely spaced isotherms, indicating conductive temperature gradients and overall low permeability in these zones. These low-permeability low-resistivity zones visible in the HTEM line appear to overlie the geothermal reservoir, similar to the patterns of low-resistivity hydrothermal smectite observed in many volcanic-hosted geothermal systems worldwide (the so-called “clay cap” model, e.g. Ussher et al., 2000; Cumming, 2016). In order to better characterize the petrologic origins of the low-resistivity zones and the specific geometries and features of the HTEM data, we conducted analysis of core and cuttings from 4 geothermal wells at DAC (labelled wells in Figure 2 and Figure 4) utilizing sample inspection, laboratory infrared reflectance spectroscopy, and methelyne blue analysis.

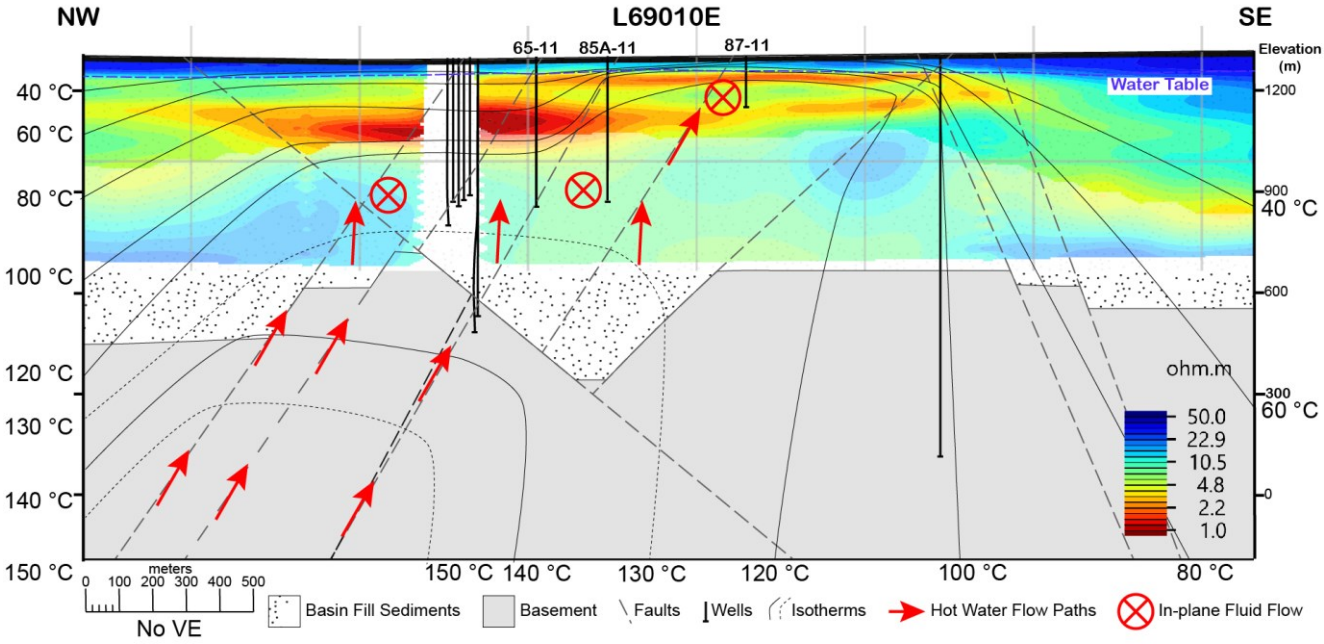

Figure 4: Conceptual model cross-section superimposed on an HTEM resistivity pattern (from line L69010E) with natural state (pre-production) inferred isotherms, hot water flow paths, and simplified geology. The gap in the HTEM profile left of center is due to interference from power plant equipment at the surface.

3. METHODS

3.1 Samples Investigated and Sample Inspection Techniques

Subsurface rock samples from four geothermal wells or boreholes from DAC were investigated (Figure 2, 4). Two of the wells (87-11, 24-12) had drill core collected (0-152.4 m total depth), and these cores were viewed, relogged using a binocular microscope, and analyzed using a portable infrared spectrometer at the Great Basin Science Samples and Records Library, operated by the Nevada Bureau of Mines and Geology. The core wells were chosen for analysis because they intersect both the high in the gravity 1VD, and the embedded resistor as observed in the HTEM data (line T69010E). The two additional wells (85A-11, 65-11) analyzed had drill cuttings collected at ~3 m (10 ft) intervals and were drilled to 433 m and 443 m depth, respectively. The cuttings samples were washed, dried, and logged on site by the mud loggers. The cuttings were analyzed using the portable infrared spectrometer at the University of Nevada, Reno, and with methylene-blue analysis at Geologica in Reno, NV. These cuttings samples were chosen because they lie along the HTEM line (T69010E) that directly crosscuts the geothermal system and they intersect low resistivity intervals. Several cuttings intervals were contaminated with Lost Circulation Materials (LCM) or there were no returns, in which case no analysis was performed on these intervals. All four wells intersect poorly sorted Quaternary-Tertiary alluvial basin fill sediment of variable grain size and variability in hydrothermal alteration mineralogy.

3.2 Laboratory Infrared Reflectance Spectroscopy

The spectrometer used in this study is a Spectral Evolution SR-5400, that measures in the Visible-Near Infrared and Short-Wave Infrared wavelength ranges (5 nm – 2500 nm). The instrument's analytical reproducibility is 0.1 nm with a wavelength accuracy from 1 to <3 nm, depending on the wavelength. Measurements were collected using a contact probe that has a field of view of 2 cm in diameter. Measurements are presented in reflectance relative to a white reference plate. White reference measurements were made at the start of data collection and every 15-20 minutes thereafter. For core, measurements were made at approximately 0.6 m increments (2 ft), targeting both representative locations and hydrothermal alteration and veining. For drill cuttings, each cuttings sample collected at ~3 m (10 ft) was analyzed with a single representative measurement.

Data processing and analysis was performed using a combination of expert driven and statistical approaches. Each spectrum was analyzed individually by a trained spectroscopist and compared to standard mineral reference libraries (such as Kokaly et al., 2017). In addition, several supervised classification algorithms were utilized using the material identification tool in the ENVI software package (Version 6.1)'s. The algorithms Spectral Angle Mapper, Euclidean Distance, and Spectral Information Divergence were utilized to aid in the identification. Each spectrum was classified as containing up to three minerals, and the subjective confidence of each classification was recorded on a scale from 1-5, with 1 being low confidence, and 5 being high confidence. In addition to mineral identification, numerical data from the spectra, known as spectral scalars, was calculated from continuum removed spectra using a python script. The continuum removal was performed using a python script by Hassanzadeh (2020), which uses the approaches by Kokaly & Clark (1999). The spectral scalars utilized in this study are the depth and wavelength position of the 1900 nm absorption feature, associated with H_2O, and the 2200 nm feature, associated with the Al-OH bond. These are used to calculate the Illite Spectral Maturity (ISM) index to estimate relative abundance of illite:smectite (Clark et al., 1990; Pontual et al., 1997; Yang et al., 2011; Simpson and Rae, 2018). Table 1 shows the calculations used for the spectral scalars discussed in the text. Simpson and Rae (2018) found that ISM values calculated from hull corrected spectra of less than 0.76 corresponded to smectite, 0.76-96 corresponded to interlayered illite smectite, and >.96 corresponded to illite without smectite based on comparison with XRD analysis. We use these numbers in our analysis, however calibration of the samples from this study through XRD analysis could improve our interpretation. The depth (or strength) or absorption features is related to abundance, as well as overall albedo and grain size (Clark et al., 1990). Here, we test the assumption that the depth of the 1900 nm feature (D:1900) is primarily a function of relative abundance, utilizing methylene-blue analysis (Section 3.3).

Table 1: Spectral scalars calculated in this study. All scalars were calculated from continuum removed spectra following Kokaly & Clark (1999). "Dxxxx:yyyy" refers to feature depth of largest feature in wavelength range xxxx to yyyy (nm). "Wuuuu:vvvv" refers to wavelength (nm) of deepest feature within wavelength range uuuu to vvvv.

Scalar Name	Calculation	Description	Source
Illite Spectral Maturity (ISM)	(1-D1800:2020) / (1-D2180:2232)	Measures ratio between Al-OH absorption and H_2O absorption features. It is related to the amount of water in the mineral structure compared to Al-OH, and can be used to estimate relative abundance of illite:smectite. Higher ISM values indicate higher illite or muscovite relative to smectite.	Similar to calculations used by Simpson and Rae, 2018; Pontual et al., 1997
Al-OH Wavelength (W:2200)	W2180:2232	This wavelength is related to illite/muscovite composition and Al-OH mineral structure	Clark et al., 1990; Yang et al., 2011
Depth of H2O feature (D:1900)	D:1800:2020	Strength of H_2O absorption in clay minerals, can approximate relative hydrated clay abundance	Clark et al., 1990

3.3 Methylene-Blue Analysis

Methylene-blue analysis is a quick and inexpensive technique used to analyze drilling muds and applied to estimate smectite content of geothermal well cuttings at the well site during drilling (Gunderson et al., 2000). The Methylene Blue (MeB) test for estimating swelling clay content utilized in this study are those of Harvey (1993) updated and annotated by Cumming (2004, 2010, 2015, 2020). One gram of each sample was ground to a consistent grain size using a coffee grinder and added to a flask with 25 ml of water and 1 ml of dilute sulfuric acid (5N). The solution was then boiled gently for 2 minutes. Following boiling, 3.74 g/l MeB solution was added at 0.5 mL increments, until the maximum amount of MeB was absorbed by the clay (as described by Harvey, 1993). The MeB solution utilized was calibrated with commercial bentonite of 60-70 % smectite and was found to be within that range (64%), therefore 1 mL of MeB is approximately 1 % smectite. Further analysis, such as comparison with clay fraction X-Ray Diffraction (XRD) analysis could better constrain the % smectite, however time and budget constraints prevented XRD validation and calibration for this project.

4. RESULTS

4.1 Mineral Identification

The following minerals were identified using infrared spectroscopy: smectite, illite, kaolinite, calcite, opal, with rare chlorite, hematite, and zeolites (Figure 5). Smectite is by far the most common mineral detected in the wells and is characterized by strong absorption

features at 1400, 1900, and 2210 nm (Figure 5A, Kokaly et al., 2017). Illite is also common in the wells, and is characterized by absorption features at 1400, 1900, 2200, and 2350 nm (Figure 5A, Kokaly et al., 2017). It is found alongside smectite, and our interpretation is that it is primarily present as interlayered illite smectite, although smectite overprinting illite could produce a similar spectral signature. Kaolinite, characterized by a distinct doublet absorption feature near 2200 nm, is uncommon in the well, and typically found at less than 50 m depth in wells 87-11 and 24-12 (Figure 5B). Opal and chalcedony, characterized by a wide absorption feature near 2200 nm were also identified (Figure 5D). In the deeper sections of the wells, a mixture of smectite, illite, calcite, and opal/chalcedony is very common (Figure 5C) and is difficult to unmix for high confidence mineral identification. Follow up XRD analysis on these samples could help better understand this mixture. In addition, an unknown mineral(s) was found in several samples from well 24-12 that had additional absorptions near 1400 nm, similar to sulfate minerals such as gypsum, alunite, and jarosite, however a match with existing library minerals was not found.

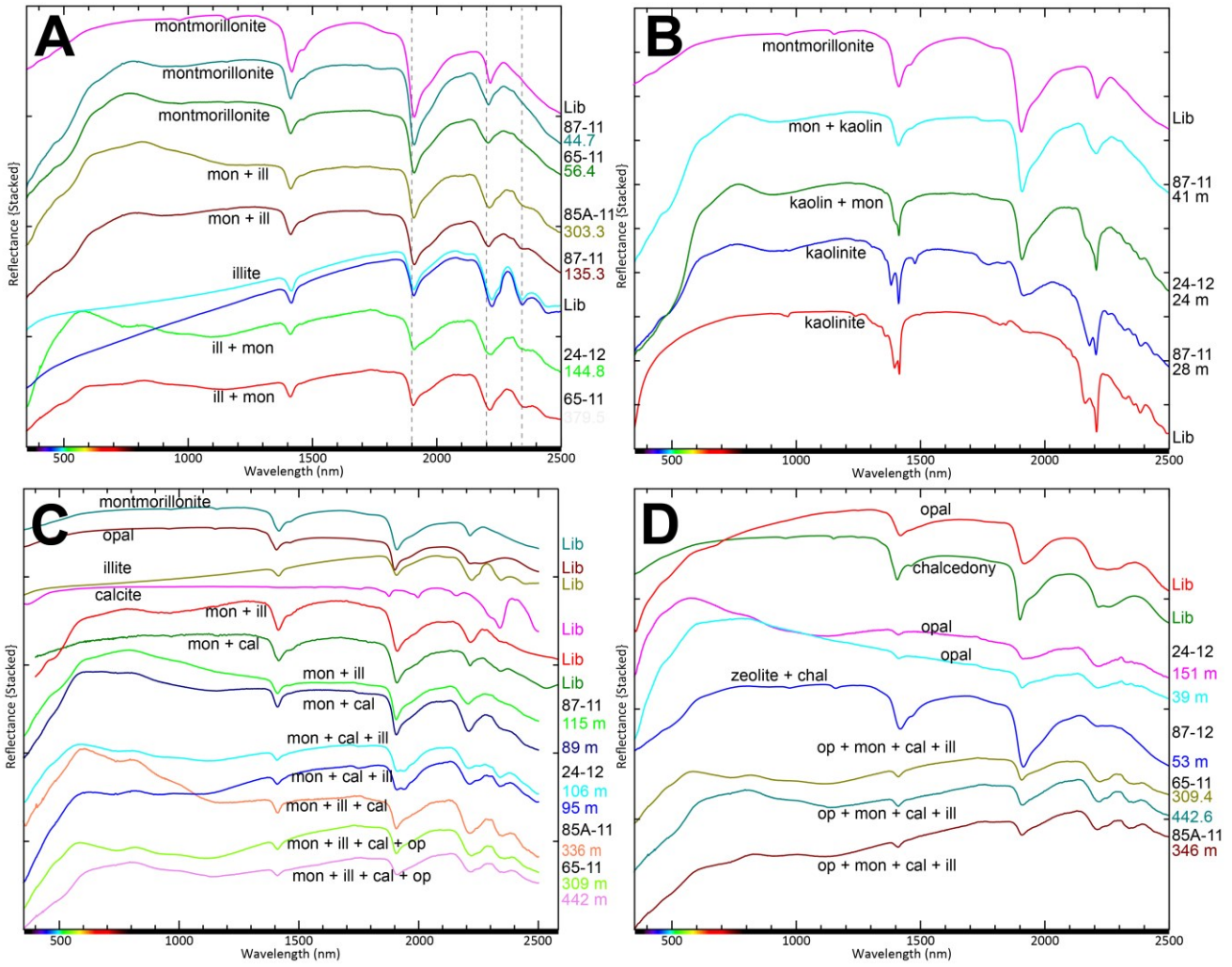

Figure 5: Representative spectra from DAC wells alongside library minerals from Kokaly et al., (2017). A: Smectite (montmorillonite) and illite, B: Kaolinite and smectite, C: Common mixtures observed (montmorillonite + opal + illite + calcite), D: Silica polymorphs (opal and chalcedony) and common mixtures measured containing opal. Side annotation: Lib refers to library mineral, and each measured spectrum is labeled with well name and depth.

The following secondary minerals were identified through sample inspection: clay, quartz and other silica polymorphs, pyrite, calcite, and hematite (e.g. Figure 6).

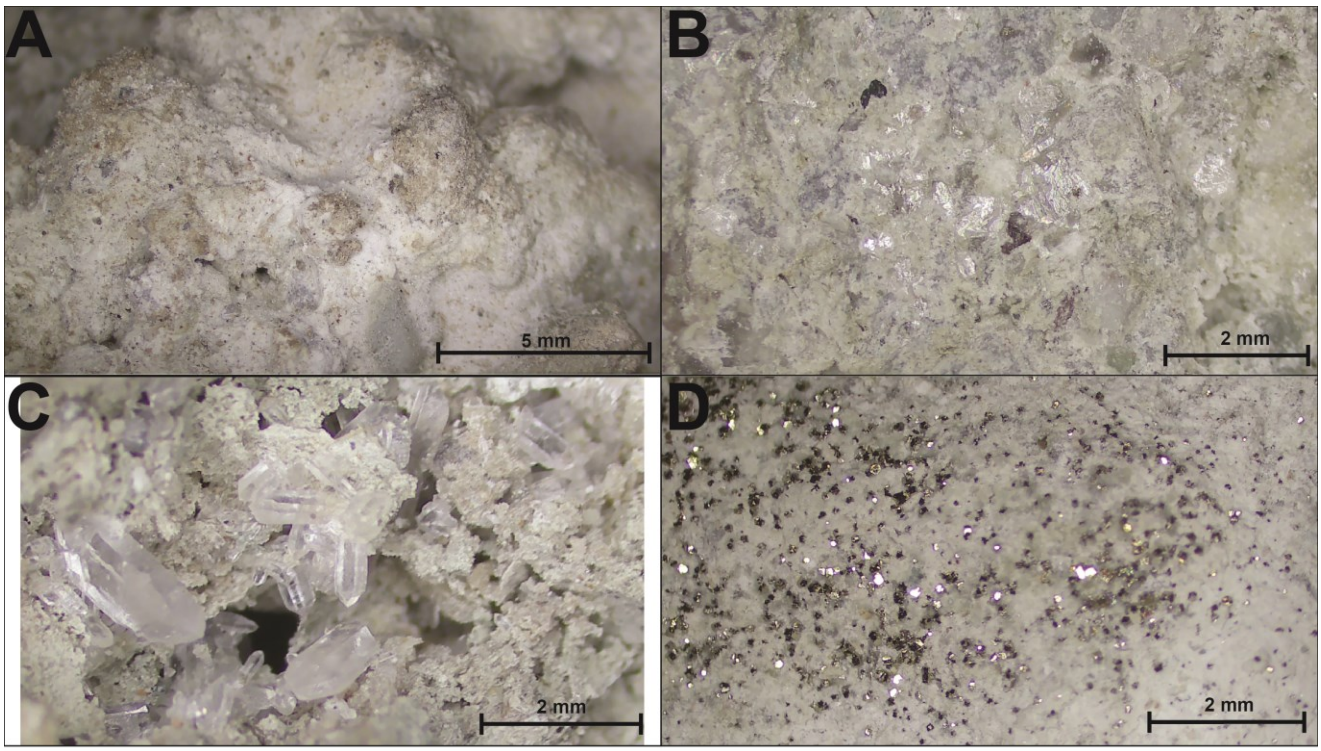

Figure 6: Example microscope images of common hydrothermal alteration minerals visible in core from DAC. A: Massive silica cementing (white) between sand grains from well 24-12, depth 372 ft, B: Massive calcite cementing from well 24-12, depth 423 ft, C: Drusy quartz in open space from well 24-12, depth 427 ft, D: Abundant pyrite accompanied by massive silica cementing observed in well 24-12, depth 387 ft.

4.2 MeB Analysis and SWIR Calibration

Table 2 shows the results of 14 MeB analyses on cuttings from wells 85A-11, and 65-11. Computed smectite amounts in the samples ranged from 1-13%. A linear correlation was observed between the MeB analysis and several of the spectral scalars (D:1900 and ISM; R^2 values of 0.9585 and 0.8644 respectively). These linear trends were utilized to calibrate a conversion equation to estimate % of smectite (or ml of MeB) from the spectral scalars alone. Here, we present the average % smectite between the two calibrations for each SWIR measurement (Figure 8-10).

Table 2: Results of MeB analysis, with spectral scalars ISM and D:1900 for reference. Each drop represents 0.5 mL of MeB solution.

SAMPLE NAME	Drop Count	Sample mass (g)	Solution Concentration (M)	Solution Amount (ml)	Smectite % Computed	ISM	D:1900
85A-11_200	11	1	0.096154	26	5.5	0.69	0.37
85A-11_230	17	1	0.096154	26	8.5	0.68	0.40
85A-11_300	10	1	0.096154	26	5	0.76	0.30
85A-11_480	9	1	0.096154	26	4.5	0.75	0.32
85A-11_610	16	1	0.096154	26	8	0.69	0.38
85A-11_750	13	1	0.096154	26	6.5	0.70	0.36
85A-11_910	12	1	0.096154	26	6	0.74	0.32
85A-11_1100	3	1	0.096154	26	1.5	0.94	0.09
85A-11_1370	2	1	0.096154	26	1	0.92	0.12
65-11_310	11	1	0.096154	26	5.5	0.71	0.34
65-11_510	18	1	0.096154	26	9	0.63	0.45
65-11_650	26	1	0.096154	26	13	0.58	0.49
65-11_980	7	1	0.096154	26	3.5	0.88	0.17

65-11_1230	6	1	0.096154	26	3	0.81	0.23

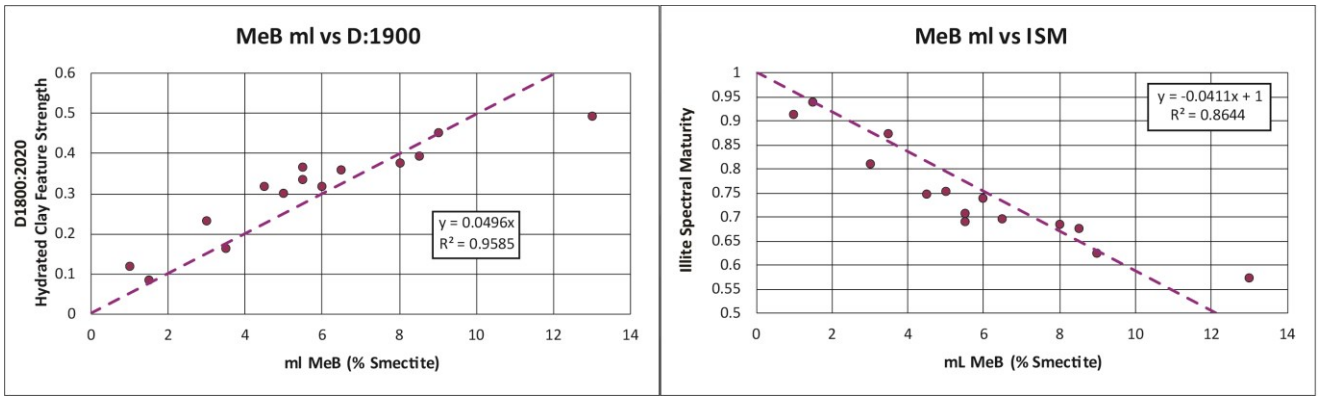

Figure 7: Methylene-blue (MeB) analysis versus spectral scalars (D:1900 and Illite Spectral Maturity, ISM) with linear regression results (set intercept of 0 and 1 respectively) used for the smectite abundance calibration.

4.3 Comparison with other downhole data and geophysics

Figure 8-10 show the results of the SWIR mineral analysis, MeB analysis, and sample inspection for the four wells investigated, as well as the temperature logs, and the extracted resistivity from the closest HTEM line (L69010E). The distance of the wells from the HTEM line varies from 22-709 m and listed in the figure caption.

For wells 85A-11 (Figure 8) and 65-11 (Figure 9), SWIR analysis of cuttings identified a general zonation of smectite, predominantly from 0~275 m depth, to interlayered illite-smectite, calcite, and silica polymorphs with rare chlorite from 275 m to total depth (~440 m). This general pattern is mirrored in spectral scalars (ISM & D:1900) and the measured and calculated % smectite based on the MeB analysis. Shallow depths (0-275 m) have higher smectite contents (5-12%), higher hydrated clay feature strength, and lower illite spectral maturity (<0.8) than the deeper interval investigated (275-440 m), characterized by lower smectite contents (0.5-5%), lower hydrated clay feature strength, and higher illite spectral maturity (0.8-1) consistent with interlayered illite-smectite. This transition at 275 m depth is also observed in the temperature data from the wells, with a transition to near isothermal temperatures of 128 °C at ~300 m. Interpretation of spectral scalars and the calculated % smectite from the MeB analysis and calibration identify additional subzones than described above, that are mirrored in the resistivity from the HTEM data. From shallow to deep in well 85A-11 (Figure 8), there is a relative high in smectite (~6-8 %) from depths between 25-75 m, which correspond to a resistivity low (2.17 ohm.m) centered around 57 m depth; a relative low in smectite (~4-6 %) between 75-150 m corresponding to a relative high (4.56 ohm.m) in resistivity at 110 m; another relative high (~7-8%) in smectite from 150-300 m corresponding to a relative low (2.45 ohm.m) in resistivity at 175 m; and finally a relative low in smectite (0.5-3%) from 300-440 m corresponding to resistivity values of ~ 7.5-7.75 ohm.m. For well 65-11, estimated smectite abundance of 4-8 % from 40-140 m correspond to resistivity values of 2.37-3.92 ohm.m, a relative high in smectite abundance (8-13 %) from 140-275 m corresponds to a low in resistivity at 175 m (1.27 ohm.m), and finally a low in smectite (1-4 %) at depths from 275-440 m corresponding to resistivity values of ~7-8.2 ohm.m.

For wells 87-11 (Figure 10) and 24-12 (Figure 11), SWIR analysis of core identified a zonation of smectite with rare kaolinite from ~0-70 m, with increasing interlayered illite-smectite, calcite, and opal to TD at ~150 m. This transition in SWIR identified minerals at ~70 m corresponds with as shift from a conductive temperature gradient profile to a near isothermal gradient at ~128 °C. For well 87-11, several distinct hydrothermal alteration zones are apparent based on SWIR mineral analysis, SWIR spectral scalars, and sample inspection (Figure 10). Zone 1, 0-45 m depth, has ~6% smectite, minor kaolinite, and calcite, a conductive temperature gradient, and a transition in resistivity from shallow high values (~15.5 ohm.m) to moderate values (~3.5 ohm.m). Zone 2, from 45-70 m, is characterized by high smectite values (6-12 %), minor silica, calcite, and hematite, a conductive temperature gradient, and a resistivity low of 2.04 ohm.m at ~ 50 m depth. Zone 3, from ~70-130 m, is characterized by relatively low estimated smectite (2-6 %), interlayered illite smectite, abundant opal and other silica polymorphs, abundant pyrite, calcite, near isothermal temperature gradients, and local high in resistivity of 5.7 ohm.m. Zone 4, from ~130-150 m, is characterized by slightly higher estimated smectite than Zone 3 (~6-10 %), more common calcite relative to silica, and slight decrease in resistivity to ~ 4 ohm.m at 150 m depth. Well 24-12 varies significantly from well 87-11, with less distinct zonation in secondary minerals, and overall lower grainsize of the host rock. In general, there is relatively high estimated smectite content (4-10 %) from 0-60 m depth, with a general decrease in smectite from 60-150 m, and generally increasing silica, pyrite, and calcite with depth. In addition, an unknown sulfate mineral is present throughout the well, here plotted as “gypsum”. There is less agreement between the smectite zonation and the HTEM resistivity in this well, and this could be because the well is significantly offset from the HTEM line (709 m) compared to the other wells.

Compared to the cuttings samples analyzed, the number of unique minerals identified is higher in the core wells, and there is more noise in the spectral scalar data overall. This is likely because the cuttings samples become relatively homogenized due to mixing during transport up the wellbore, and with possible contamination from shallower portions of the well. This could lead to less unique mineral identifications in cuttings than from the core due to less common minerals being missed. A similar pattern is observed between cuttings and sidewall core collected at the Fallon FORGE EGS site from same well (Kraal & Ayling, 2019; Kraal et al., 2021). It is also possible

that there could be mineralogical differences between the cuttings and core wells, due to intersecting different lithologies and/or hydrothermal alteration zones. This would be consistent with the geophysics and conceptual model, where the core wells intersect a high in the gravity 1VD, inferred to be caused by shallow hydrothermal alteration processes (precipitation of dense secondary minerals in shallow basin fills sediments).

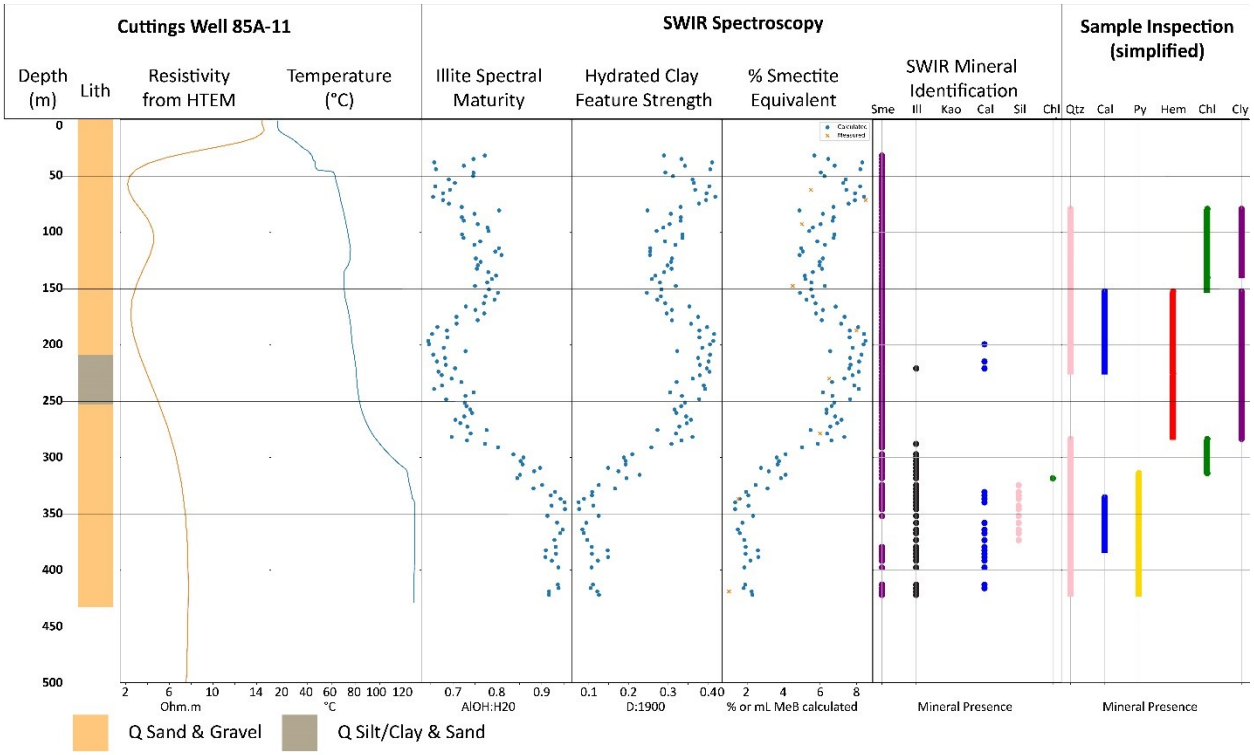

Figure 8: Downhole well logs from well 85A-11, including lithology, resistivity from closest HTEM line, temperature, and SWIR spectroscopy analysis. The projected HTEM line is 294 m from the well. Sme refers to Smectite, Ill refers to Illite, Kao refers to Kaolin group minerals, Sil refers to Silica (Opal, Chalcedony, Quartz), Chl refers to Chlorite, Cal refers to Calcite, Py refers to Pyrite, Hem refers to Hematite, and Cly refers to Clay.

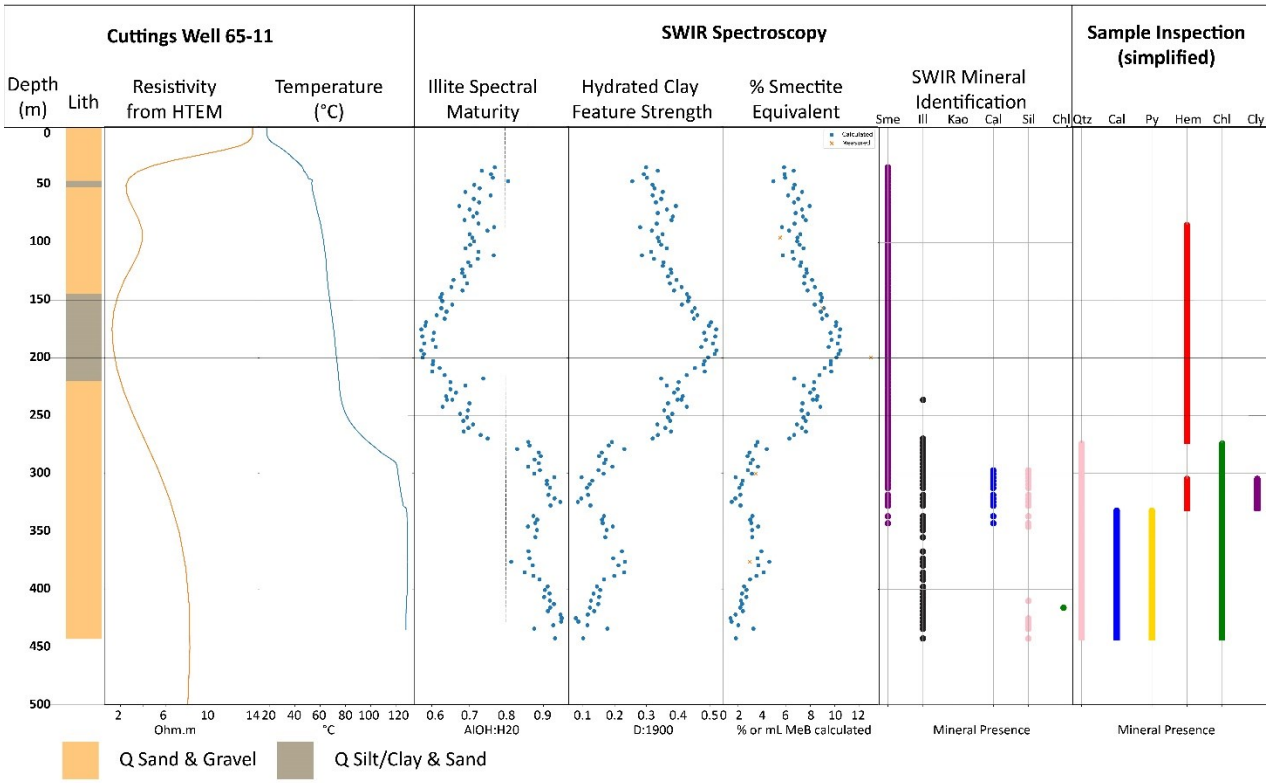

Figure 9: Downhole well logs from well 65-11, including lithology, resistivity from closest HTEM line, temperature, and SWIR spectroscopy analysis. The projected HTEM line is 103 m from the well. Refer to Figure 8 for mineral legend.

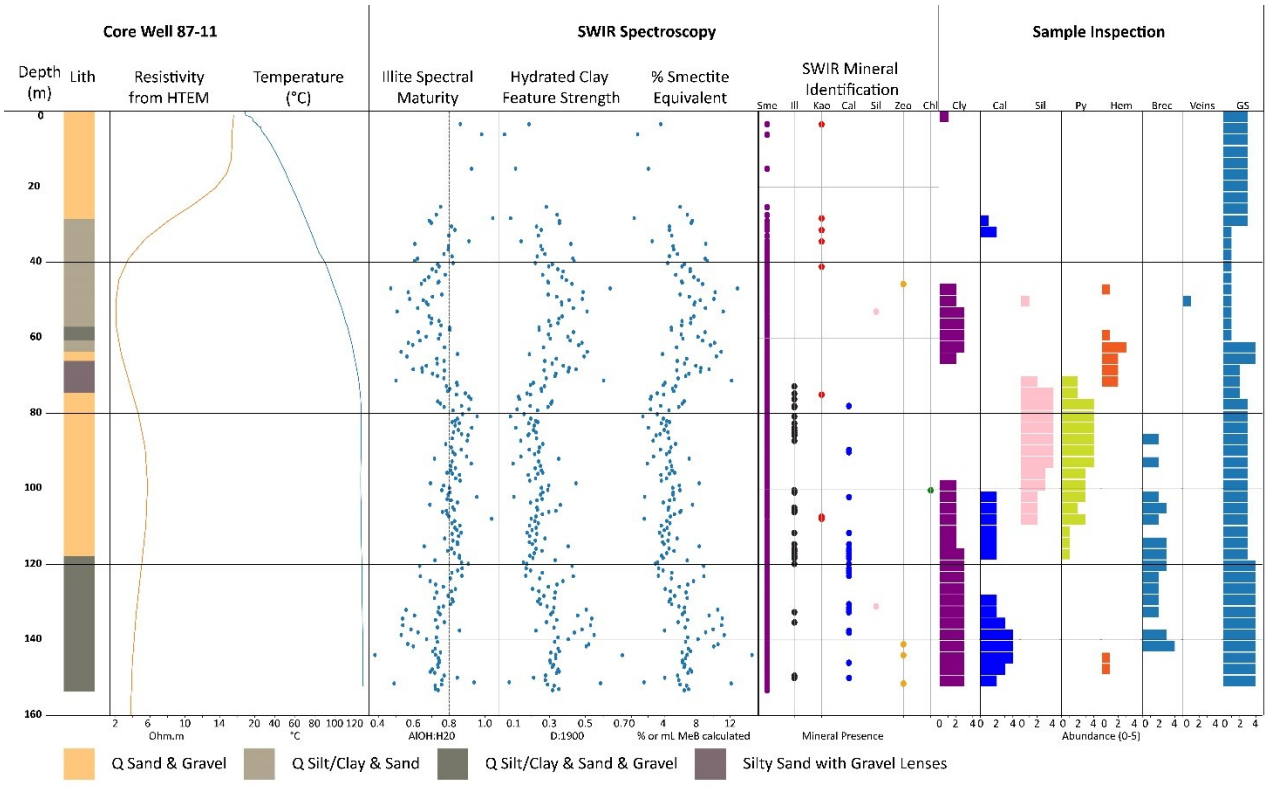

Figure 10: Downhole well logs from well 87-11, including lithology, resistivity from closest HTEM line, temperature, SWIR spectroscopy analysis, and secondary minerals, brecciation, veins, and overall grainsize observed. The projected HTEM line is 22 m from the well. Zeo refers to Zeolite, Brecc refers to Brecciation, and GS refers to grain size, refer to Figure 8 for additional abreviations.

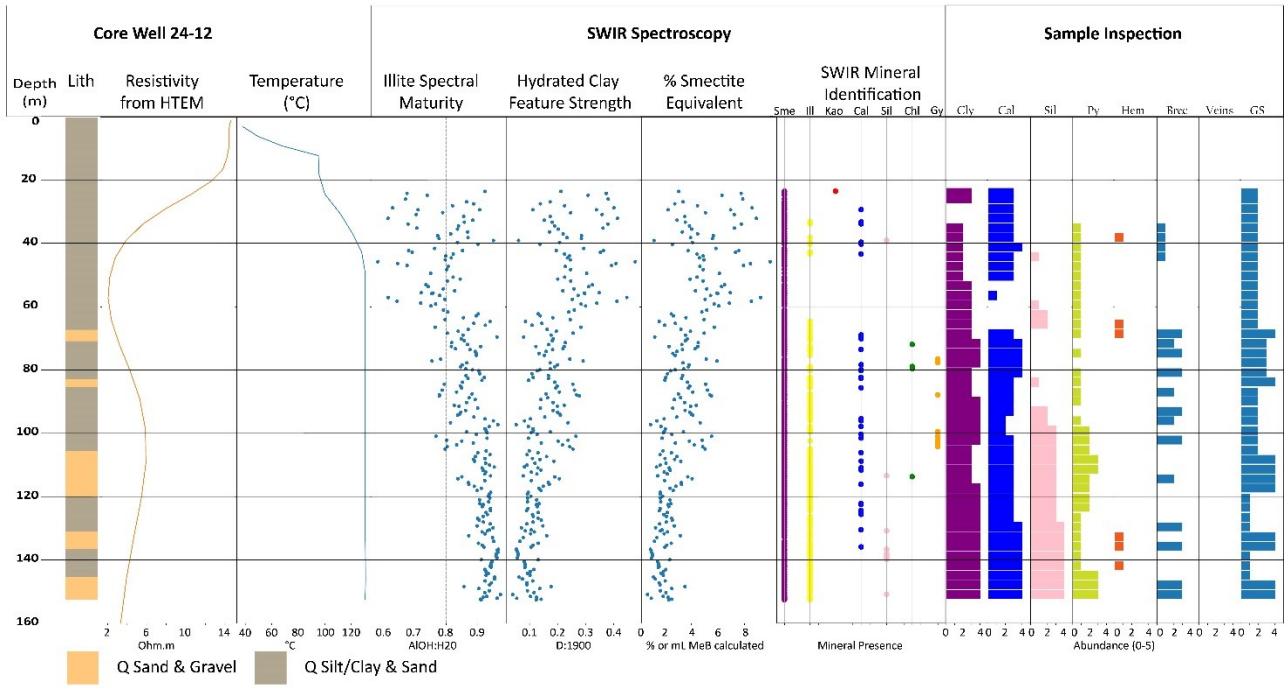

Figure 11: Downhole well logs from well 24-12, including lithology, resistivity from closest HTEM line, temperature, SWIR spectroscopy analysis, and secondary minerals, brecciation, veins, and overall grainsize observed. The projected HTEM line is 709 m from the well. Gy refers to Gypsum (or unknown sulfate mineral, see text for details). Refer to Figure 10 for additional abbreviations.

5. DISCUSSION

5.1 Genetic model of hydrothermal mineral formation at DAC, resulting geophysical signature, and conceptual model.

As seen in section 3.3, there is a strong relationship between resistivity as observed in the HTEM line(s) and the smectite content of the wells that intersect the line, as well as the secondary minerals observed, such as silica, calcite, and pyrite. Our interpretation is that these minerals are present due to hydrothermal alteration of the basin fill sediments by the geothermal fluids. Smectite is a typical hydrothermal alteration product of neutral pH hydrothermal fluids at less than 180 °C (Browne, 1978; Henley & Ellis, 1983; Reyes, 1990). Interlayed illite-smectite is most common at higher temperatures in volcanic environments (180-225 °C), but has been present at lower temperatures down to ~150 °C, although smectite is usually more predomanent. The typical temperature range for interlayered illite-smectite is higher than currently observed at Don A Campbell (~130 °C max temperatures in basin fill sediments). There are several possible interpretations for the presence of illite: A) the system was hotter in the past, and the interlayered illite-smectite is a relict mineral from this previous hotter period, B) interlayered illite-smectite stability may be possible at lower temperatures when hosted in basin fill sediments, C) the illite was present in the primary rock and is not a product of hydrothermal alteration, or D) the current interpretation of the SWIR mineralogy incorrectly identified a mixture of smectite, calcite, and silica as also containing illite. Our prefered interpretations is that there is a combination of scenario A and B. We will discuss the four possibilities below.

It is likely that the system may have been hotter in the past. Relict high temperature alteration minerals have been observed at most geothermal fields where detailed hydrothermal mineral characterization has taken place, such as those in volcanic environments of the Phillipines, New Zealand, and the Geysers, USA (e.g. Reyes, 1990; Chambefort et al., 2017; Walters et al., 1991; Moore et al., 2000) as well as in deep-circulation type systems in the U.S. Great Basin at Desert Peak (Lutz et al., 2009), and the Tungsten Mountain geothermal field (Kraal, 2023). It appears that many hydrothermal systems display cyclicle qualities, with initial vigorous activity and slow decline in both temperature and permeability, often followed by reinvigoration (e.g. Lutz et al., 2002). Mechanisms for temperature decline are exhaustion of heat source (e.g. from the magma body in volcanic hosted systems), decline in permeability (often due to precipitation of vein filling minerals; e.g. Rimstidt & Barnes, 1980; Fournier, 1989; Sibson, 1987; Elders et al., 1979), and cold water influx leading to collapse of the system. Mechanisms for reinvigoration are intrusion of new magma bodies providing heat (for volcanic hosted systems), and creation/maintanence of new fracture permeability through faulting and earthquake activity (e.g. Sibson, 1987; 2000; Siler et al., 2023). A lowering of the water table such as those due to climatic factors, fault-driven uplift, or valley incision could also lead to the overprinting of deeper (higher-temperature) alteration minerals by shallower (low-temperature) minerals (e.g. Sillitoe 2015).

Temperature stability ranges commonly used for interpretation of geothermal minerals, such as those referenced above (e.g. Browne, 1978; Henley & Ellis, 1983; and Reyes 1990) are based primarily from emperical studies of active geothermal systems in high temperature volcanic environments, and to a lesser extent based on laboratory water-rock interaction experiments and numerical modeling. It is possible that further work analyzing hydrothermal altertion mineral zonation in low-moderate temperature geothermal

systems hosted in basins may find differnet temperature ranges than those conducted in high temperature volcanic environments due to variability in fluid and rock chemical composition between these end members.

It is possible that variability in the basin-fill sediment provinance may play a role in the resistivity structure and smectite content observed, however, the low resistivity zone corresponding to high smectite content appears to be directly co-located with the extent of the active geothermal system, and therefore it seems likely that former is a product of the latter. Petrographic analyis, such as described by Stimac (2023) through observation under polarized light, or utilizing Scanning Electron Microscopy could better understand the origin of the hydrothermal alteration minerals, their paragenesis, and more information about the original sediment sources. However, it is also likely that sediment grain size and composition can play a role in shallow hydrothermal fluid flow, where coarser grained high permeability units (e.g. fanglomerates, beach deposits) provide shallow fluid flow pathways, and fine-grained deposits (such as lake sediments) provide barriers. Hydrothermal alteration processes could further modify the permeability and porosity of these sediment end members through the precipitation of secondary minerals.

Lastly, it is possible that there is a mineral mixture misidentification, therefore a follow-up XRD study on the clay sized fraction of the cuttings analyzed could further confirm our interpretation of the SWIR data. However, best practices were utilized for high precision identification of minerals using laboratory SWIR spectroscopy, including statistical methodologies for spectra matching, as well as visual confirmation of each match by a spectroscopist. Previous work by the authors (Kraal et al., 2021; 2023a; 2023b) and others (e.g. Calvin and Pace, 2016; Simpson and Rae, 2018) find general agreement between SWIR mineral identifications and other methods such as petrographic microscopy and XRD.

In addition to the contributions of smectite and illite-smectite to the geophysical signature of the site, the precipitation of silica polymorphs, calcite, and pyrite also have an effect. The near surface embedded resistor and the near surface densification infered from the gravity 1VD could be the product of the precipitation of silica and calcite. Silica polymorphs (opal, chalcedony, quartz) are common alteration products from a cooling silica saturated fluid (Fournier, 1985a). Calcite, with reverse solubility, can either be precipitated from a cooling geothermal fluid when boiling, or through heating of cold CO_2-rich groundwater at the margins of the system (Fournier, 1985b;). Both minerals would increase the density of the basin fill sediments, and raise the resistivity. Pyrite is a common secondary mineral ubiquitous to geothermal systems with a wide temperature stability range (Browne, 1978; Henley & Ellis, 1983; and Reyes 1990). Pyrite is found at DAC in highest abundance alongside silicification. Hematite is often formed in hydrothermal environments through oxidation of secondary pyrite, sometimes near the water table in the steam heated zone (Sillitoe, 2015). At DAC, hematite is most abundant in the shallow portions of wells associated with areas of high smectite concentration, possibly formed through the oxidation of pyrite.

Figure 12 is a conceptual model diagram along the HTEM line L69010E based on our interpretation of the well data, and geophysical results, showing several hydrothermal alteration mineral zones hosted in the basin fill sediments. The main hydrothermal alteration zones are as follows: 1) an argillic zone composed of abundant smectite (5-13 % based on MeB analysis) commonly found with hematite, resistivity values of less than 3 ohm.m, and generally conductive temperature gradients (infered from closely spaced isotherms) due to overall low permeability (the “clay cap”); 2) a shallow silicified and calcified zone characterized by lower smectite contents (2-5%) likely present as interlayered illite-smectite, found alongside abundant pyrite, and likely relatively high permeability infered from near-isothermal temperature profiles through this zone, interpretted to correspond to a shallow outflow zone; 3) a larger deeper silicified zone, with silica alteration most abundant along northwest-dipping normal faults, with abundant pyrite, calcite, and lesser interlayered illite-smectite (smectite <2%), and chlorite with overall high permeability as infered by the frequent mudlosses in these intervals, and the target for production and injection wells in the field; 4) a thin kaolinite + smectite + hematite zone with minor calcite above the argillic zone at and near the current water table, potentially formed from steam-heated advanced argillic overprinting of smectite above the shallow outflow reservior hosted in the embedded silicified zone. Normal faults within the basin-fill sediments are infered to provide additional fracture permeability and flow pathways for the hydrothermal fluids, perhaps providing a pathway through the argillic “clay cap” from the deeper silicified zone to the shallow silicified zone (Figure 12). The shallow outflow zone may also take advantage of existing higher-permeability sediments, or fracture permeability due to faulting, evident by the presence of coarser sediments in this zone (Figure 10), and normal faulting adjacent to the shallow core wells (Figure 2).

While wells through the shallow outflow zone infered within the embeded resistor remain isothermal and do not have temperature reversals as expected for a shallow outflow, outflow is plausable based on the following observations: the embedded resistor is where near-boiling fluids come closest to the water table, it has unique alteration as per this study, is in a relatively permeable horizon, and is located over a hotter part of the reservoir. If the lower conductor is less permeable, and as it is sandwiched in between two hot things, it will come into equilibrium with them and therefore we would not expect a thermal overturn. The outflow direction is uncertain. The northeast flow direction inferred here is based on the geometry of the shallow temperature anomaly, the northeast trending high in the gravity 1VD data, and the presence of thermal overturns in wells to the northeast of the study area (Figure 2).

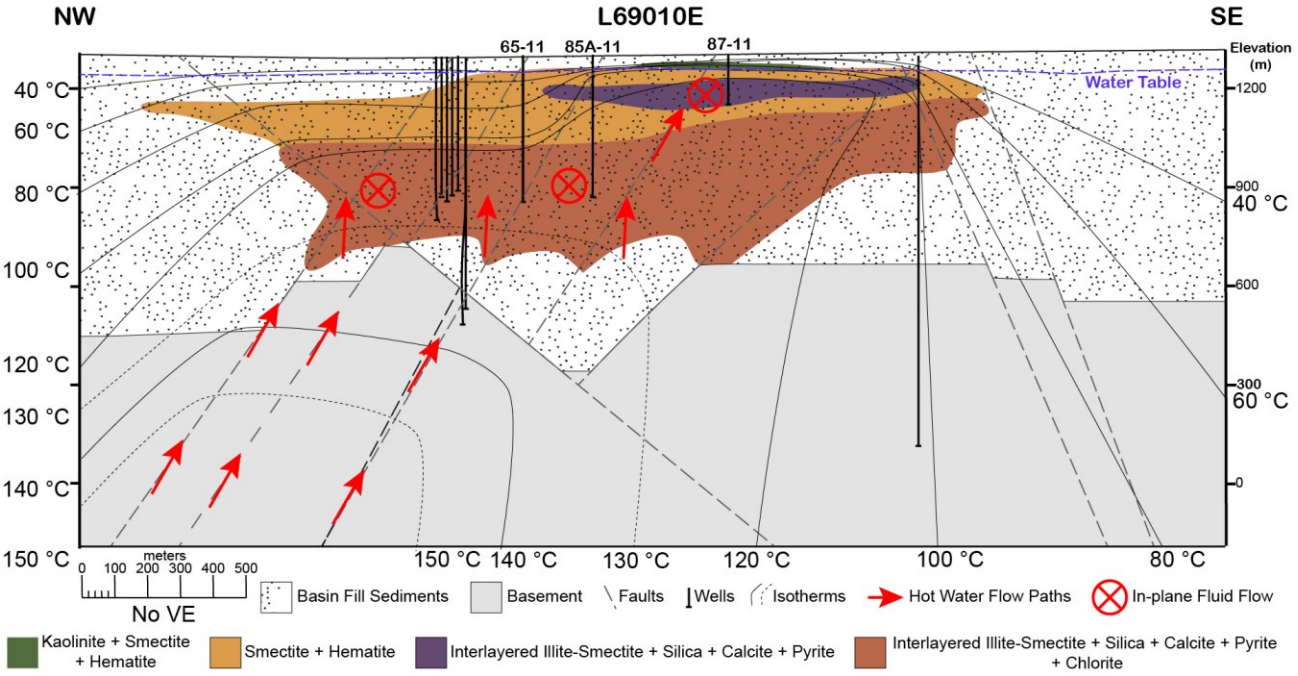

Figure 12: Conceptual model of D.A.C. with alteration zones hosted in basin fill sediments inferred from well mineral analysis and interpretation of HTEM resistivity data (Figure 3).

5.2 Comparison with other geothermal fields in the basin and range, implications for exploration, and generalized conceptual model.

The DAC geothermal system has many analogues in the Great Basin region, as well as in western Turkey where deep-circulation type systems predominate. In addition, DAC is a blind geothermal system, and therefore is similar to many of the undiscovered geothermal resources in the region. Therefore, our interpretation of the relationship between geophysical anomalies and hydrothermal alteration mineralogy zonation can be applied to many of these systems. Structural analogues to DAC, hosted in displacement transfer zones between kinematically linked strike-slip and normal faults, include Blue Mountain, and Wabuska in Nevada. Well characterized prospects without current power production hosted in displacement transfer zones include East Hawthorne, Petrified Springs/South Gabbs, and potentially Lee-Allen, also in Nevada. DAC is relatively unique in the B&R region due to the producing geothermal reservoir being hosted completely within Quaternary-Tertiary alluvial sediments at natural state temperatures ~130 °C. However, several other power-producing systems utilize shallow reservoirs for either production or injection, such as San Emidio and Salt Wells. Shallow low-resistivity zones are associated with nearly every examined system in the region, including the prospects of East Hawthorne, Lee-Allen, Grover Point, Petrified Springs/Southeast Gabbs, and developed fields like Desert Peak, San Emidio, Tungsten Mountain, Steamboat and Salt Wells (e.g. Sewell et al., 2023; Craig et al., 2021; Folsom et al., 2020; 2023; 2024; Kraal, 2023a; Feucht et al., 2023; Downs et al., 2025) however most of these do not have detailed petrological analysis to compare with the geophysics data. If our interpretation from DAC can be applied to these analogous areas, then the existence of hydrothermal smectite forming low-resistivity zones above or adjacent to active power-capable hydrothermal systems is relatively common. One feature that is shared between several of the sites (DAC, San Emidio, Grover Point, and Lee-Allen) is an embedded or shallow resistive zone within the low-resistivity cap. This has been observed be consistent with shallow silicification and shallow outflow at DAC and San Emidio, and exploration drilling at Grover Point and Lee-Allen may reveal similar patterns there.

6. CONCLUSION

Shallow low resistivity zones are commonly found above active geothermal systems in the Basin and Range region, and are key for utilizing resistivity techniques, such as HTEM, for greenfield exploration. This work shows that these low-resistivity (~1-5 ohm.m) zones at the DAC geothermal field are co-located with abundant smectite (5-13%), and intermediate (~5-10 ohm.m) resistivity zones co-located with silicification or calcification, and interlayered illite-smectite clays rather than smectite. Further petrologic work, such as XRD, thin section petrography, SEM analysis, and Raman Spectroscopy could further validate our interpretation, and provide context and petrogenesis information for the minerals identified in this study.

ACKNOWLEDGMENTS

This material was based upon work supported by the U.S. Department of Energy, Office of Energy Efficiency and Renewable Energy (EERE), Office of Technology Development, Geothermal Technologies Office under the FY2020 Hydrothermal and Low Temperature Multi-Topic Funding Opportunity Announcement DE-FOA-0002219. Sandia National Laboratories is a multi-mission laboratory managed and operated by National Technology & Engineering Solutions of Sandia, LLC, a wholly owned subsidiary of Honeywell

International Inc., for the U.S. Department of Energy's National Nuclear Security Administration under contract DENA0003525. This paper describes objective technical results and analysis. Any subjective views or opinions that might be expressed in the paper do not necessarily represent the views of the U.S. Department of Energy or the United States Government. The United States Government retains, and the publisher, by accepting the article for publication, acknowledges that the United States Government retains a non-exclusive, paid-up, irrevocable, world-wide license to publish or reproduce the published form of this manuscript, or allow others to do so, for United States Government purposes. Thank you to Wendy Calvin at University of Nevada Reno for use of the portable SWIR spectrometer utilized in this study. We would also like to thank Ormat Technologies INC for collaboration and data share.

REFERENCES

Allis, R. G. (1990). Geophysical anomalies over epithermal systems. Journal of Geochemical Exploration, 36(1-3), 339-374.

Benoit, W. R., Hiner, J. E., & Forest, R. T. (1982). Discovery and geology of the Desert Peak geothermal field: A case history. Bulletin 97 (No. NP-4900578). Nevada University, Reno (USA).

Browne, P. R. L. (1978). Hydrothermal alteration in active geothermal fields. Annual Review of Earth and Planetary Sciences, 6(1), 229-248.

Calvin, W. M., & Pace, E. L. (2016). Alteration in geothermal drill core using a field-portable spectroradiometer. Geothermics, 61, 12-23.

Chambefort, I., Lewis, B., Simpson, M. P., Bignall, G., Rae, A. J., & Ganefanto, N. (2017). Ngatamariki geothermal system: Magmatic to epithermal transition in the Taupo volcanic zone, New Zealand. Economic Geology, 113(2), 319-346.

Clark, R. N., King, T. V., Klejwa, M., Swayze, G. A., & Vergo, N. (1990). High spectral resolution reflectance spectroscopy of minerals. Journal of Geophysical Research: Solid Earth, 95(B8), 12653-12680.

Craig, J. W., Faulds, J. E., Hinz, N. H., Earney, T. E., Schermerhorn, W. D., Siler, D. L., ... & Deoreo, S. B. (2021). Discovery and analysis of a blind geothermal system in southeastern Gabbs Valley, western Nevada, USA. Geothermics, 97, 102177.

Delwiche, B. (2013). Exploration of the Wild Rose geothermal project, Mineral County, Nevada. In Nevada Petroleum and Geothermal Society Field Trip Guide: Geothermal and petroleum developments in several extensional basins of the central Walker Lane, Nevada (pp. 13-27).

Delwiche, B., Libbey, R., Folsom, M., Johnson, A., Murphy, J., & Zuza, R. (2023). Exploration history and conceptual model of the Dixie Meadows geothermal field, Nevada, USA. In Proceedings World Geothermal Congress 2023, Beijing, China, April 17-21.

Downs, C., Schwering, P., Sewell, S., Winn, C., Hinz, N., Zimmerman, J., Blake, K., Sabin, A., Lopeman, J., Milton, A., Siler, D., & Cumming, W. (2023). Development of the Prospect Portfolio and initial surface exploration studies in the Basin & Range Investigations for Developing Geothermal Energy (BRIDGE) Project. GRC Transactions, 47.

Downs, C., Winn, C., Kraal, K., Folsom, M., Zimmerman, J., Sewell, S., Cumming, W., Milton, A., Hinz, N., Schwering, P., Sabin, A., & Lopeman, J. (2025). Basin & Range Investigations for Developing Geothermal Energy (BRIDGE). Final Technical Report. DOE Contract Number NA0003525.

Elders, W. A., Hoagland, J. R., McDowell, S. D., & Cobo, J. M. (1979). Hydrothermal mineral zones in the geothermal reservoir of Cerro Prieto. Geothermics, 8(3-4), 201-209.

ENVI software (6.1). Retrieved from https://www.l3harrisgeospatial.com/

Feucht, D., Gates, C., Selwood, R., Churchill, M., & Zuza, R. (2023). Magnetotelluric data acquisition in a high-noise environment: Results from the Steamboat Hills geothermal complex, Nevada, USA. GRC Transactions, 47.

Folsom, M., Lopeman, J., Perkin, D., & Sophy, M. (2018, February). Imaging shallow outflow alteration to locate productive faults in Ormat's Brady's and Desert Peak fields using CSAMT. In Proceedings of the 43rd Workshop on Geothermal Reservoir Engineering (pp. 12-14). Stanford, CA, USA.

Folsom, M., Libbey, R., Feucht, D., Warren, I., & Garanzini, S. (2020, February). Geophysical observations and integrated conceptual models of the San Emidio geothermal field, Nevada. In Proceedings of the 45th Workshop on Geothermal Reservoir Engineering (pp. 21p). Stanford University, Stanford, CA, USA.

Folsom, M., Winn, C., Milton, A., Zimmerman, J., Blake, K., Sabin, A., Downs, C., Sewell, S., Kraal, K., Nale, S., & Huang, W. C. (2023). An early-stage exploration update on the Grover Point blind geothermal system in Dixie Valley, Nevada: Highlights of geophysics results and conceptual modeling. In Proceedings, 49th Workshop on Geothermal Reservoir Engineering (SGP-TR-227). Stanford University, Stanford, California.

Folsom, M., Sewell, S., Cumming, W., Zimmerman, J., Sabin, A., Downs, C., Hinz, N., Winn, C., Seiderman, B., & Schwering, P. (2024). A direct comparison of resistivity models from helicopter transient electromagnetic and magnetotelluric datasets collected over a blind geothermal system in East Hawthorne, Nevada, USA. GRC Transactions, 48.

Fournier, R. O. (1985a). The behavior of silica in hydrothermal solutions. In B. R. Berger, P. M. Bethke, & J. M. Robertson (Eds.), Geology and geochemistry of epithermal systems (Vol. 2). Society of Economic Geologists. https://doi.org/10.5382/Rev.02

Fournier, R. O. (1985b). Carbonate transport and deposition in the epithermal environment. In B. R. Berger, P. M. Bethke, & J. M. Robertson (Eds.), Geology and geochemistry of epithermal systems (Vol. 2). Society of Economic Geologists. https://doi.org/10.5382/Rev.02

Fournier, R. O. (1989). Geochemistry and dynamics of the Yellowstone National Park hydrothermal system. Annual Review of Earth and Planetary Sciences, 17(1), 13-53.

Glaas, C., Vidal, J., Patrier, P., Girard, J. F., Beaufort, D., Petit, S., & Genter, A. (2019). How do secondary minerals in granite help distinguish paleo-from present-day permeable fracture zones? Joint interpretation of SWIR spectroscopy and geophysical logs in the geothermal wells of Northern Alsace. Geofluids, 2019.

Glen, J. M., & Earney, T. E. (2024). GeoDAWN: Airborne magnetic and radiometric surveys of the northwestern Great Basin, Nevada and California. USGS Data Release. https://doi.org/10.5066/P93LGLVQ

Hassanzadeh, A. (2020). yxoos/ContinuumRemoval: Zenodo Release (1.0). Zenodo. https://doi.org/10.5281/zenodo.3612622

Henley, R. W., & Ellis, A. J. (1983). Geothermal systems ancient and modern: A geochemical review. Earth-Science Reviews, 19(1), 1-50.

Jowitt, S. M., Micander, R., Richards, M., Fisher, T., Reynolds, D., & Lu, C. (2024). The Nevada mineral industry 2023. Nevada Bureau of Mines and Geology Special Publication MI-2023, 96 p.

Kokaly, R. F., & Clark, R. N. (1999). Spectroscopic determination of leaf biochemistry using band-depth analysis of absorption features and stepwise multiple linear regression. Remote Sensing of Environment, 67(3), 267-287.

Kokaly, R. F., Clark, R. N., Swayze, G. A., Livo, K. E., Hoefen, T. M., Pearson, N. C., ... & Klein, A. J. (2017). USGS spectral library version 7 (No. 1035). US Geological Survey.

Kraal, K. O., Ayling, B. F., Blake, K., Hackett, L., Perdana, T. S. P., & Stacey, R. (2021). Linkages between hydrothermal alteration, natural fractures, and permeability: Integration of borehole data for reservoir characterization at the Fallon FORGE EGS site, Nevada, USA. Geothermics, 89, 101946.

Kraal, K. O. (2023a). Application of hydrothermal alteration mineral analysis to geothermal reservoir characterization for three geothermal fields in the western United States (Doctoral dissertation, University of Nevada, Reno).

Kraal, K. O., Ayling, B. F., DeOreo, S., & Calvin, W. (2023b). Infrared spectroscopy as a tool for hydrothermal alteration mineral analysis to support geothermal reservoir characterization at The Geysers, CA, USA. Journal of Volcanology and Geothermal Research, 445, 107968.

Kratt, C., Coolbaugh, M., Sladek, C., Zehner, R., Penfield, R., & Delwiche, B. (2008). A new gold pan for the West: Discovering blind geothermal systems with shallow temperature surveys. GRC Transactions, 32, 153-158.

Lutz, S. J., Caskey, S. J., Mildenhall, D. D., Browne, P. R. L., & Johnson, S. D. (2002, January). Dating sinter deposits in northern Dixie Valley, Nevada—The paleoseismic record and implications for the Dixie Valley geothermal system. In Proceedings 27th Workshop on Geothermal Reservoir Engineering (pp. 284-290).

Lutz, S., Moore, J., Jones, C., Suemnicht, G., & Robertson-Tait, A. (2009, February). Geological and structural relationships in the Desert Peak geothermal system, Nevada: Implications for EGS development. In Proceedings 34th Workshop on Geothermal Reservoir Engineering.

Moore, J. N., Adams, M. C., & Anderson, A. J. (2000). The fluid inclusion and mineralogic record of the transition from liquid-to vapor-dominated conditions in the Geysers geothermal system, California. Economic Geology, 95(8), 1719-1737.

Orenstein, R., & Delwiche, B. (2014). The Don A. Campbell geothermal project. GRC Transactions, 38, 91-97.

Payne, J. F. (2013). Characterization of a blind geothermal prospect through LiDAR analysis and shallow temperature survey, Gabbs Valley, Nye and Mineral Co., NV (Master's thesis, University of Nevada Reno).

Pontual, S., Merry, N., & Gamson, P. (1997). Spectral interpretation field manual: Spectral analysis guide for mineral exploration 1.

Reyes, A. G. (1990). Petrology of Philippine geothermal systems and the application of alteration mineralogy to their assessment. Journal of Volcanology and Geothermal Research, 43, 279-309.

Rimstidt, J. D., & Barnes, H. L. (1980). The kinetics of silica-water reactions. Geochimica et Cosmochimica Acta, 44(11), 1683-1699.

Savitri, K. P. (2024). Spectral analysis for geothermal exploration: A method investigation to bring the technology closer to geothermal community (PhD thesis, University of Twente, Faculty of Geo-Information Science and Earth Observation). https://doi.org/10.3990/1.9789036562034

Sewell, S., Cumming, W., Schwering, P., Hinz, P., Downs, C., Zimmerman, J., Bedrosian, P., Robinson, B., Murray, D., & Schultz, A. (2023). Using helicopter time-domain electromagnetic (HTEM) resistivity surveys with supporting geoscience data to target temperature gradient wells and discover hidden geothermal systems in the US Basin and Range. GRC Transactions, 47.

Sibson, R. H. (1987). Earthquake rupturing as a mineralizing agent in hydrothermal systems. Geology, 15(8), 701-704.

Sibson, R. H. (2000). Fluid involvement in normal faulting. Journal of Geodynamics, 29(3-5), 469-499.

Siler, D. L. (2023). Structural discontinuities and their control on hydrothermal systems in the Great Basin, USA. Geoenergy, 1(1), geoenergy2023-009.

Sillitoe, R. H. (2015). Epithermal paleosurfaces. Mineralium Deposita, 50(7), 767-793.

Simpson, M. P., & Rae, A. J. (2018). Short-wave infrared (SWIR) reflectance spectrometric characterization of clays from geothermal systems of the Taupo Volcanic Zone, New Zealand. Geothermics, 73, 74-90.

Stimac, J. (2023). Petrography as a cost-effective approach to understanding geothermal system evolution. GRC Transactions, 47, 1034911.

Thompson, A. J. B., Hauff, P. L., & Robitaille, A. J. (1999). Alteration mapping in exploration: Application of shortwave infrared (SWIR) spectroscopy. Society of Economic Geologists Newsletters, 39, 16–27.

Ussher, G., Harvey, C., Johnstone, R., & Anderson, E. (2000, May). Understanding the resistivities observed in geothermal systems. In Proceedings World Geothermal Congress (pp. 1915-1920). Kyushu, Japan.

Vest Christiansen, A., & Auken, E. (2012). A global measure for depth of investigation. Geophysics, 77(4), WB171-WB177.

Walters, M. A., Sternfeld, J. N., Haizlip, J. R., Drenick, A. F., & Combs, J. (1991). A vapor-dominated high-temperature reservoir at the Geysers, California. Geothermal Resources Council, Monograph on The Geysers Geothermal Field, Special Report No. 17.

Winn, C., Dobson, P., Ulrich, C., Kneafsey, T., Lowry, T., Akerley, J., ... & Bauer, S. (2021). Lost circulation in a hydrothermally cemented basin-fill reservoir: Don A. Campbell geothermal field, Nevada (No. SAND2021-7728C). Sandia National Lab. (SNL-NM), Albuquerque, NM (United States).

Winn, C., Dobson, P., Ulrich, C., Kneafsey, T., Lowry, T. S., Akerley, J., ... & Bauer, S. (2023). Context and mitigation of lost circulation during geothermal drilling in diverse geologic settings. Geothermics, 108, 102630.

Yang, K., Huntington, J. F., Browne, P. R., & Ma, C. (2000). An infrared spectral reflectance study of hydrothermal alteration minerals from the Te Mihi sector of the Wairakei geothermal system, New Zealand. Geothermics, 29(3), 377-392.

Yang, K., Browne, P. R. L., Huntington, J. F., & Walshe, J. L. (2001). Characterising the hydrothermal alteration of the Broadlands–Ohaaki geothermal system, New Zealand, using short-wave infrared spectroscopy. Journal of Volcanology and Geothermal Research, 106(1-2), 53-65.

Yang, K., Huntington, J. F., Gemmell, J. B., & Scott, K. M. (2011). Variations in composition and abundance of white mica in the hydrothermal alteration system at Hellyer, Tasmania, as revealed by infrared reflectance spectroscopy. Journal of Geochemical Exploration, 108(2), 143-156.